Organically Capped Iridium Nanoparticles as High-Performance Bifunctional Electrocatalysts for Full Water Splitting in Both Acidic and Alkaline Media: Impacts of Metal−Ligand Interfacial Interactions

Yi Peng, Qiming Liu, Bingzhang Lu, Ting He, Forrest Nichols, Xiao Hu, Tiffanie Huang, Grace Huang, Lizette Guzman, Yuan Ping,* and Shaowei Chen*

Read Online

ACCESS | Metrics & More | Article Recommendations | SI Supporting Information

ABSTRACT: Design and engineering of bifunctional catalysts are critical in the development of electrochemical full water splitting. In this study, 4-ethylphenylacetylene-functionalized iridium (Ir−C≡, 1.7 ± 0.3 nm in diameter) nanoparticles are found to exhibit markedly enhanced electrocatalytic activity toward both hydrogen and oxygen evolution reactions (HER and OER) in acidic and alkaline media, in comparison to the nanoparticles capped with mercapto and nitrene derivatives. Remarkably, the HER and OER performances in alkaline media are even better than those of commercial Ir/C and Pt/C benchmarks. This is accounted for by the formation of Ir−C≡C− conjugated interfacial linkage that leads to significant intraparticle charge delocalization and hence manipulation of the electron density of the Ir nanoparticles and interactions with key reaction intermediates. This is indeed confirmed by results from both spectroscopic measurements and density functional theory calculations. With Ir−C≡ nanoparticles as both the cathode and anode catalysts for electrochemical water splitting, a low cell voltage of 1.495 and 1.473 V is needed to reach the current density of 10 mA cm^{-2} in alkaline and acidic media, respectively. Such a performance is markedly better than that of commercial Ir/C (1.548 and 1.561 V) and relevant catalysts reported in recent literature, highlighting the significance of interfacial engineering in the development of high-performance bifunctional electrocatalysts.

KEYWORDS: *iridium nanoparticle, acetylene, interfacial bond, hydrogen evolution reaction, oxygen evolution reaction, full water splitting*
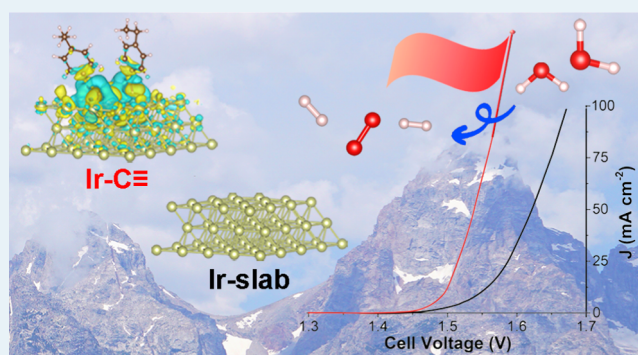
INTRODUCTION

Electrochemical water splitting represents a unique technology for the sustainable production of hydrogen and oxygen by the hydrogen evolution reaction (HER) at the cathode and oxygen evolution reaction (OER) at the anode under mild conditions, respectively.[1,2] However, both HER and OER necessitate the employment of appropriate catalysts, so as to achieve a sufficiently high current density for practical applications. Currently, Pt/C is the benchmark electrocatalyst for HER, whereas RuO$_2$ and IrO$_2$ are the benchmark electrocatalysts for OER.[3] It would be of fundamental and technological significance to develop bifunctional electrocatalysts that are active toward both HER and OER, so as to significantly reduce the costs of catalyst synthesis and electrode fabrication, a critical aspect in practical commercialization.[4] Indeed, a range of nanomaterials, such as non-noble metals, metal oxides/carbide/sulfides, and carbon-based composites, have been examined as bifunctional electrocatalysts.[5−9] However, their performances have mostly remained subpar, compared to those

of the benchmark electrocatalysts and do not meet the requirement for practical applications.[10−23]

Fundamentally, it has been demonstrated that the strength of hydrogen and oxygen binding to the respective electrocatalytic active site is a critical parameter for HER and OER. In fact, the H binding energy (ΔG_{H*}) has been used as a unique descriptor to evaluate the HER performance within the framework of a so-called "volcano plot".[24,25] For Ir, the ΔG_{H*} is situated on the left side of the volcano plot, suggesting that the binding of H to Ir is slightly too strong, and thus, the surface electron density of Ir needs to be lowered somewhat, so
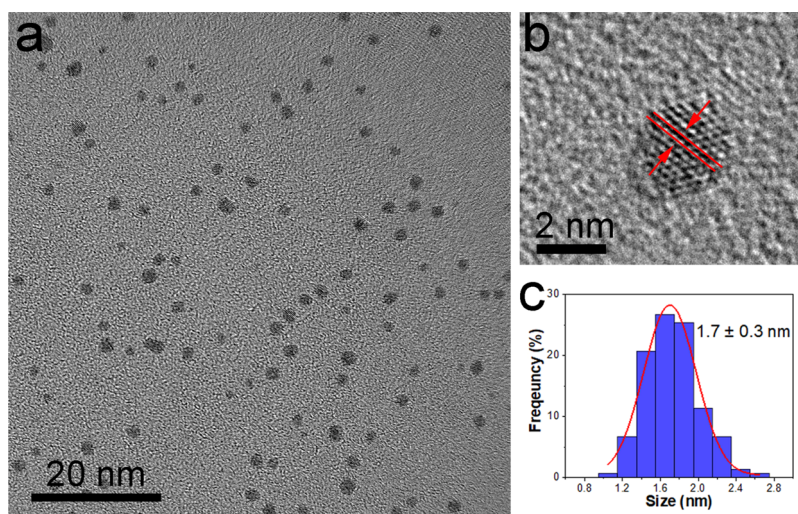
Figure 1. (a,b) TEM images of Ir nanoparticles and (c) the corresponding core size histogram.

as to reach the optimal peak. As for OER, prior research has shown that metallic Ir is prone to be oxidized at high electrode potentials, and low-valence IrO_x actually exhibits a higher electrocatalytic activity than the high-valence counterparts,[21,26] suggesting that a reduced oxidation state of Ir is desired for enhanced OER performance. This can be achieved by structural engineering that leads to a decreased O binding energy,[27] typically within the context of nanoparticle size, shape, morphology, and alloying.[3,28−34] For instance, Zhu et al.[35] prepared Pd@Ir-nL core−shell nanocubes (n = 1−4, the number of atomic Ir layers) and observed maximal OER performance at n = 3, with an overpotential ($\eta_{10,OER}$) of only +245 mV to reach the current density of 10 mA·cm^{-2} and a mass activity of 3.33 A mg$_{Ir}^{-1}$ at η = +300 mV, which was markedly better than that of commercial Ir/C, because of Pd−Ir intermixing and possible ligand and/or strain effects. In another study,[36] by alloying with tungsten (W, a 5d metal), IrW nanobranches were prepared and used as bifunctional electrocatalysts for full water splitting, where a cell voltage (E_{10}) of 1.58 and 1.60 V was needed to reach 10 mA·cm^{-2} in 0.1 M HClO$_4$ and 0.1 M KOH, respectively, which was 120 and 130 mV lower than that with commercial Ir because of the changed electronic structure of Ir by W. In addition, the electrocatalytic activity can also be manipulated by strong interactions with the supporting substrates, such as carbon-based materials.[37,38] For instance, Wu et al.[21] prepared ultrasmall Ir nanoparticles supported on N-doped graphene (Ir@N-G-750) and observed a cell voltage of 1.6 V for overall water splitting at 20 mA·cm^{-2} in 0.1 M HClO$_4$, because of the formation of abundant Ir−N coordination sites. Cao and co-workers[22] prepared cucurbit[6]uril-stabilized Ir nanoparticles, which showed an E_{10} of 1.56 V in full water splitting in 0.1 M HClO$_4$ and long-term stability, because of the coordination interaction between Ir and cucurbit[6]uril that facilitated the formation and stabilization of surface active species.

In a series of earlier studies,[39,40] we demonstrated that deliberate functionalization of metal nanoparticles with select organic ligands can be exploited as an additional, powerful variable in manipulating the surface electron density and hence electrocatalytic activity toward a range of important reactions, such as the oxygen reduction reaction and formic acid oxidation. For example, it has been shown that the electron-withdrawing/donating property of the para-substituted groups

of phenyl ligands can manipulate the nanoparticle's surface electronic structure and hence the electrocatalytic activity, because of effective metal−ligand interfacial charge transfer.[41,42] In the present study, we demonstrate that by surface functionalization of Ir nanoparticles with acetylene derivatives, the resulting Ir nanoparticles can be used as high-performance electrocatalysts toward both HER and OER in both acidic and alkaline media (with the alkaline HER and OER activity significantly better than that of commercial Pt/C and Ir/C). This is ascribed to the formation of conjugated Ir−C≡ metal−ligand interfacial bonding interactions that reduces the electron density of the Ir nanoparticles and the interactions with critical reaction intermediates, in comparison to the mercapto- (Ir−S) and nitrene-capped (Ir=N) counterparts. In fact, the Ir−C≡ nanoparticles can be used as both anode and cathode catalysts for full water splitting, which displays a low E_{10} of only 1.495 and 1.473 V in alkaline and acidic media, respectively. Such a performance is markedly better than that of commercial Ir/C (1.548 and 1.561 V).

■ RESULTS AND DISCUSSION

Organically capped Ir nanoparticles were synthesized by adopting a procedure used previously based on controlled thermolysis and subsequent ligand exchange (details in the Experimental Section).[43,44] It involves two major steps (Scheme S1). "Bare" Ir nanoparticles were first prepared by thermolytic reduction of IrCl$_3$ in 1,2-propanediol in the presence of sodium acetate and then were functionalized with 4-ethylphenylacetylene (EPA), 4-ethylphenylthiol (EPT), or 4-dodecylbenzenesulfonyl azide (DBSA) by ligand exchange. The resulting nanoparticles were denoted as Ir−C≡, Ir−S, and Ir=N, respectively, reflecting the formation of such metal−ligand interfacial bonds. The structures of the nanoparticles were first studied by transmission electron microscopic (TEM) measurements. From the TEM image in Figure 1a, one can see that the Ir nanoparticles were well dispersed on the TEM grid without apparent agglomeration, and in high-resolution measurements (Figure 1b), well-defined lattice fringes can be readily identified, with an interplanar spacing of ca. 0.225 nm that is consistent with the Ir(111) facets (JCPDS card no. 46-1044).[45] Statistical analysis based on more than 100 nanoparticles showed that the nanoparticles were mostly in the narrow range of 1.4−2.0 nm in diameter,

averaging 1.7 ± 0.3 nm, as depicted in the core size histogram in Figure 1c.

The optical properties of the nanoparticles were then examined by spectroscopic measurements. From Figure S1a, the Ir−C≡, Ir−S, and Ir═N nanoparticles can be seen to exhibit a similar exponential decay profile in UV−vis absorption measurements, consistent with the nanosized structure,[46] but markedly different photoluminescence emissions (Figure S1b). Specifically, when excited by 335 nm irradiation, Ir−C≡ exhibited an apparent emission centered at 388 nm. This is attributed to the intraparticle charge delocalization arising from the conjugated Ir−C≡C− interfacial bonds.[44,47] Ir═N displayed a broad, weak emission centered at 425 nm, because of the formation of conjugated Ir═N interfacial linkages.[48,49] By contrast, only a featureless profile was observed with the Ir−S sample, because of the formation of only nonconjugated interfacial bonds and lack of intraparticle charge delocalization. Consistent results were obtained in Fourier transform infrared (FTIR) measurements (Figure S2).[39]

The valence states of the nanoparticles were then studied by X-ray photoelectron spectroscopy (XPS) measurements. Figure 2a depicts the high-resolution scans of the Ir 4f electrons of the three nanoparticle samples, which all entail a doublet with a spin−orbit coupling of 2.90 eV that is consistent with that of Ir(0).[50] However, the exact binding energies of the $4f_{7/2}/4f_{5/2}$ doublet vary among the samples, at 60.84/83.74 eV for Ir−S, 61.76/83.66 eV for Ir═N, and 61.51/84.41 eV for Ir−C≡, that is, in comparison to Ir−S, the Ir═N and Ir−C≡ nanoparticles exhibited a positive shift of 0.92 and 0.67 eV, respectively, of the Ir 4f binding energy, suggesting charge transfer from the metal core to the respective ligands, most likely because of the formation of conjugated metal−ligand interfacial bonds, as observed previously.[39] Consistent results were obtained in the evaluation of the valence band maximum (VBM) of the respective nanoparticles (Figure 2b), where the Ir−S sample can be seen to exhibit the lowest VBM at about −0.81 eV, in comparison to +0.07 eV for Ir═N and −0.15 eV for Ir−C≡. This suggests that the d-band centers of the latter two samples shift markedly toward the Fermi level, as compared to the former.[51−53]

Consistent results were obtained from density functional theory (DFT) calculations. An Ir(111) slab was adopted based on the TEM results (Figure 1b), and two ligands of −C≡C−, ═N−SO₂−, and −S-substituted ethylbenzene were anchored onto the slab and relaxed to the optimal structure. The respective models are shown in the top panels of Figure 2c. It should be noted that in Ir═N−, two O atoms (red) of the sulfonyl group also participated in the interfacial anchoring. Notably, analysis of the charge density distributions (bottom panels) shows that interfacial charge transfer occurred in all three structures from the Ir slab to the organic capping ligands; however, the extent of charge transfer varied. Specifically, a gain of 0.87, 1.75, and 0.36 electrons for ligands based on Bader charge analysis was observed for the Ir−C≡, Ir═N, and Ir−S structure, respectively, highlighting the significance of conjugated interfacial bonding interactions in facilitating metal−ligand change transfer (Figure S3), as observed above in XPS measurements.

With such apparent manipulation of the electronic properties of the Ir nanoparticles by the organic capping ligands (Figure 2), significant enhancement was indeed observed of the electrocatalytic activities toward both HER and OER. Figure 3a shows the HER polarization curves in 1.0 M KOH of the Ir−S, Ir═N, and Ir−C≡ nanoparticles, along with commercial 20 wt % Ir/C as the benchmark. One can see that all samples exhibited non-zero currents as the electrode potential was swept negatively. However, the activity varied significantly among the samples. For instance, the overpotential ($\eta_{10,HER}$) needed to reach the current density of 10 mA cm⁻² is markedly different, at −237, −74, −38, and only −7 mV for Ir−S, Ir═N, Ir/C, and Ir−C≡, respectively. That is, the Ir−C≡ sample stood out as the best among the series and even outperformed commercial Ir/C by a large margin (Figure S4a). Of particular note is that the $\eta_{10,HER}$ of Ir−C≡ (−7 mV in 1.0 M KOH) was even significantly lower than leading results in recent literature, such as Ir@N-G-750 (−43 mV),[21] Co@Ir/NC (−121 mV),[37] RuC$_x$N$_y$ single-atom catalysts (−12 mV),[54] and commercial Pt/C (−49 mV).[54] The corresponding Tafel plots are shown in Figure 3b, and the slope was found to decrease in the order of Ir−S (182 mV dec⁻¹) > Ir═N (91 mV dec⁻¹) > Ir/C (71 mV dec⁻¹) > Ir−C≡ (62 mV dec⁻¹). This indicates that the kinetics of HER on Ir−C≡ was the fastest among the series of catalysts, following mostly the Volmer−Heyrovsky pathway.[55,56] Consistent results were obtained in electrochemical impedance spectroscopy (EIS) measurements. From the Nyquist plots in Figure S5a, the Ir−C≡ sample was found to exhibit the lowest charge
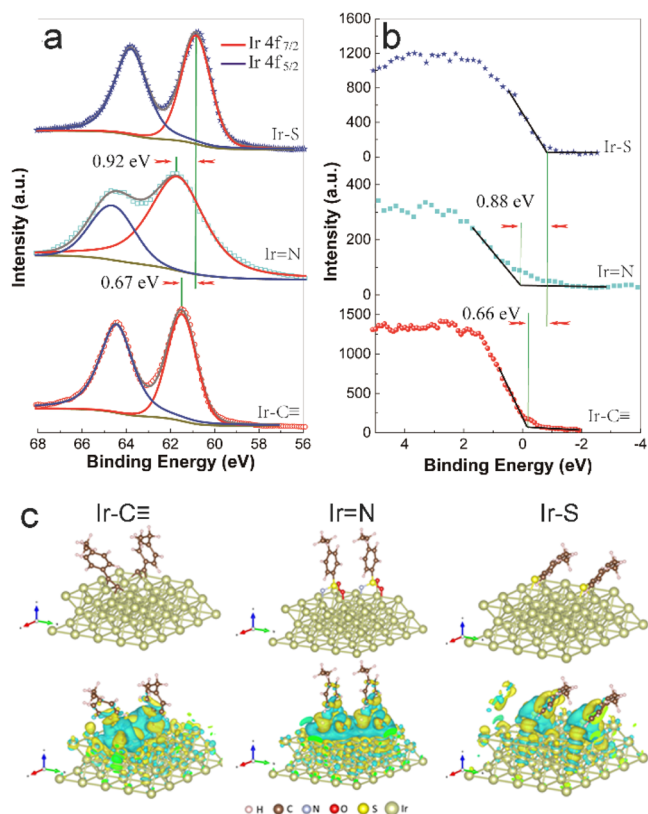

Figure 2. Interfacial charge transfer characterizations. (a) High-resolution XPS profiles of the Ir 4f electrons of Ir−C≡, Ir═N, and Ir−S nanoparticles and (b) corresponding spectra of the VBM. (c) (Top panels) Optimized structures of Ir−C≡, Ir═N, and Ir−S slabs and (bottom panels) the corresponding interfacial charge density distributions. The cyan and yellow areas signify electron loss and electron gain, respectively. The isovalue of charge density is 0.001 e/au³.
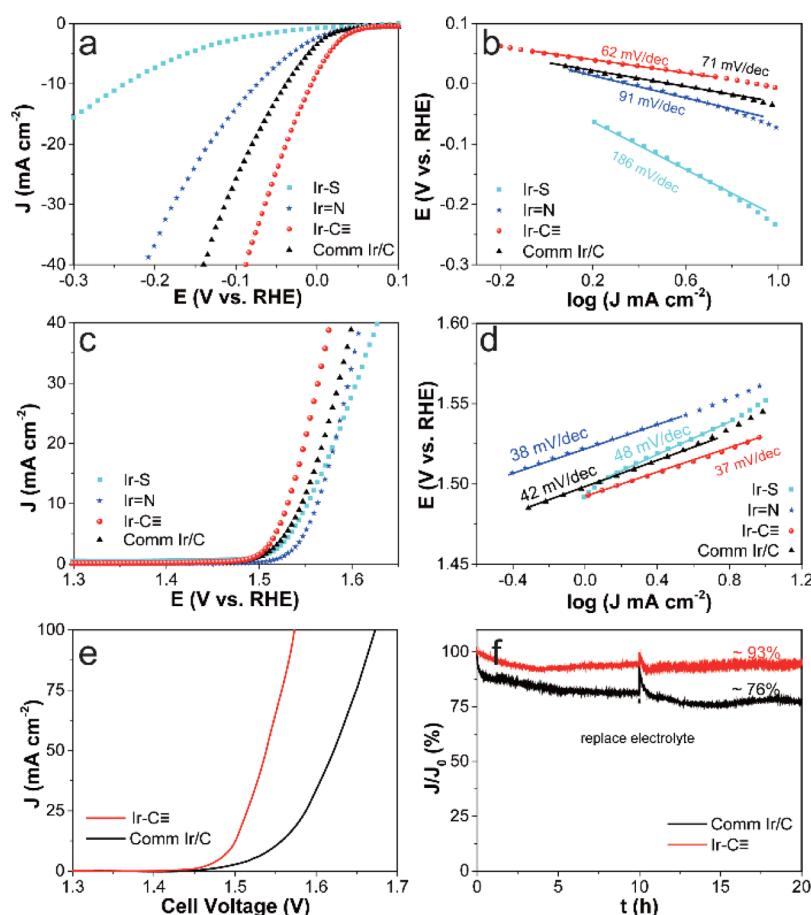
Figure 3. Bifunctional electrocatalytic performance toward HER and OER in 1.0 M KOH. (a) HER polarization curves of the series of electrocatalysts and (b) the corresponding Tafel plots. (c) OER polarization curves of the series of electrocatalysts and (d) the corresponding Tafel plots. (e) Current−voltage profiles of overall water splitting with Ir−C≡ and commercial Ir/C as bifunctional electrocatalysts in 1.0 M KOH and (f) corresponding activity retention tests by CA measurements at the respective initial E_{10}.

transfer resistance (R_{ct} = 6.6 Ω) among the series (10.8 Ω for Ir/C, 24.1 Ω for Ir═N, and 173.6 Ω for Ir−S).

The OER performance of the samples was also analyzed and compared in a similar manner. From the polarization curves in Figure 3c, one can see that all samples were apparently active toward OER, but $\eta_{10,OER}$ differed substantially, at +300, +316, +333, and +322 mV for Ir−C≡, Ir/C, Ir═N, and Ir−S, respectively, with a corresponding Tafel slope of 37, 42, 38, and 48 mV dec^{-1}. This indicates that the Ir−C≡ nanoparticles also exhibited the best OER performance among the series (Figure S4b). Note that the Tafel slope of Ir−C≡ is even markedly lower than that of relevant Ir-based catalysts reported in earlier studies (mostly greater than 50 mV dec^{-1}) in alkaline media,[21,36,37] indicating the unique advantage of surface functionalization of Ir nanoparticles by acetylene derivatives in enhancing the OER kinetics. Consistent results were obtained in EIS measurements, where the Ir−C≡ sample also exhibited the lowest R_{ct} (11.0 Ω) among the series (13.3, 23.5, and 44.8 Ω for Ir/C, Ir−S, and Ir═N, respectively, Figure S5b). Notably, the OER performance is actually comparable or superior to results of leading catalysts reported in the literature, such as IrW,[36] Co@Ir/NC,[37] IrO$_x$,[57−59] and noble metal-free catalysts.[60,61]

With such remarkable activities toward both HER and OER, the Ir−C≡ nanoparticles can be used as effective bifunctional catalysts for full water splitting, as demonstrated by the production of a large number of bubbles on both the cathode

and anode (Movie S1). From Figure 3e, the E_{10} can be estimated to be merely 1.495 V, which is 54 mV lower than that of commercial Ir/C. In fact, Ir−C≡ outperformed a large number of Ir-based bifunctional catalysts for full water splitting in alkaline media that were reported recently in the literature (Table S1). Notably, the Ir−C≡ catalysts also exhibited excellent stability. Figure 3f depicts the current profiles of full water splitting during continuous operation for 20 h. One can see that about 93% of the initial current density was retained with Ir−C≡, markedly higher than that (76%) for commercial Ir/C, suggesting enhanced long-term stability of the former. Indeed, the Ir−C≡ sample exhibited virtually no change in the current−voltage profiles before and after the stability test, whereas a drastic anodic shift was observed for Ir/C (Figure S6).

Remarkably, the Ir−C≡ nanoparticles also exhibited a markedly better performance toward both HER and OER in acidic media than others in the series (Figures S7−S9). For HER in 0.5 M H$_2$SO$_4$, the $\eta_{10,HER}$, Tafel slope, and R_{ct} were the lowest for Ir−C≡ at −33 mV, 26 mV dec^{-1}, and 8.3 Ω, respectively, in comparison to −55 mV, 28 mV dec^{-1}, and 39.3 Ω for commercial Ir/C, −98 mV, 67 mV dec^{-1}, and 122.0 Ω for Ir═N, and −154 mV, 90 mV dec^{-1}, and 278.1 Ω for Ir−S. Similarly, for OER in 0.5 M H$_2$SO$_4$, Ir−C≡ exhibited an $\eta_{10,OER}$ of +256 mV, a Tafel slope of 55 mV dec^{-1}, and an R_{ct} of 4.8 Ω, a performance much better than that of commercial Ir/ C (+291 mV, 55 mV dec^{-1}, and 7.1 Ω), Ir═N (+268 mV, 52
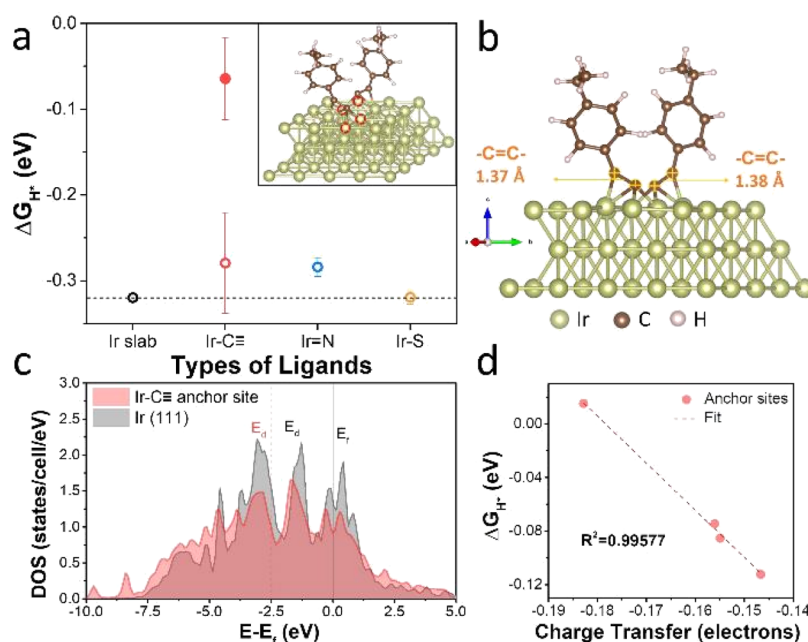
Figure 4. DFT calculation results of HER. (a) Averaged Gibbs free energy of H* adsorption (ΔG_{H*}) on ligand-anchoring Ir atoms (solid spheres) and the neighboring Ir atoms (hollow spheres) in different organically modified Ir(111) slabs and bare Ir(111) slabs. Error bars reflect variations among similar sites. The inset shows the relaxed Ir−C≡ structure and the ligand-anchoring Ir atoms circled in red. (b) Structural configuration of the relaxed Ir−C≡ model. (c) PDOS and d band center (E_d) of ligand-anchoring Ir and bare Ir(111). (d) Linear correlation between the charge transfer from ligand-anchoring Ir atoms to the ligand and their ΔG_{H*}. The four data points are for the adsorption sites highlighted in panel (a).

mV dec^{-1}, and 8.3 Ω), and Ir−S (+417 mV, 104 mV dec^{-1}, and 28.0 Ω). In addition, using Ir−C≡ as bifunctional catalysts for acidic electrochemical water splitting, the E_{10} was only 1.473 V, 88 mV lower than that of commercial Ir/C (1.561 V), and more than 80% of the initial current density was retained after 8 h of continuous operation, in comparison to an almost 90% loss with commercial Ir/C. The enhanced stability of Ir−C≡ over Ir/C is also clearly manifested by comparing the polarization curves before and after the stability tests (Figure S10). From these results, one can see that Ir−C≡ can indeed serve as a high-performance bifunctional catalyst toward electrochemical water splitting in both acidic and alkaline media (Table S1).

To unravel the mechanistic insights into the remarkably enhanced electrocatalytic performance by organic capping ligands, ΔG_{H*}, a commonly used descriptor of HER activity, was calculated using the models consisting of an Ir(111) slab capped with varied organic ligands (Figure 2c). As the interfacial charge transfer was mostly confined between the organic ligands and the ligand-anchoring and neighboring Ir sites, only these sites were considered for H adsorption (which are marked in Figure S11), and the corresponding ΔG_{H*} was ccalculated. Meanwhile, monodentate adsorption of H* was adopted in this study because of the high H* coverage, as manifested in Tafel analysis (Figure 3b).[62] From Figure 4a, one can see that $|\Delta G_{H*}|$ is very large at ca. 0.320 eV on the bare Ir(111) slab, consistent with the limited HER activity of Ir/C, and becomes slightly lower (0.279 ± 0.059 eV) for the Ir sites neighboring ligand anchoring in Ir−C≡, whereas for the ligand-anchoring Ir sites, the $|\Delta G_{H*}|$ is drastically diminished to only 0.064 ± 0.048 eV (Table S2), suggesting that the latter sites (inset of Figure 4a) are most likely responsible for the remarkable HER activity observed above for Ir−C≡ (Figures 3 and S7). It should be noted that upon the binding of the acetylene ligand onto the Ir slab, the −C≡C− bond length

increased from ca. 1.2 to 1.38 Å (Figures 4b and S12). Such a decrease in the bond order is consistent with the intraparticle charge delocalization arising from the conjugated interfacial bonds.[39,44,63,64] By contrast, a very consistent ΔG_{H*} was observed at the neighboring Ir sites when the Ir slab was capped with either mercapto or nitrene ligands (Table S2), which was estimated to be −0.319 ± 0.007 eV for Ir−S and decreased slightly to −0.284 ± 0.010 eV for Ir═N (note that no stable adsorption of H can be observed on the ligand-anchoring Ir sites of Ir═N or Ir−S, data not shown). Overall, the fact that $|\Delta G_{H*}|$ varies in the order of Ir−C≡ < Ir═N < Ir−S is in excellent agreement with the variation in the HER activity observed experimentally in both acidic and alkaline media (Figures 3 and S7).

The weakened H* adsorption (i.e., diminished $|\Delta G_{H*}|$) observed with the Ir−C≡ ligand anchoring sites is also manifested in the shift of the d band center (E_d) to −2.59 from −2.08 eV of the bare Ir(111) slab, as shown in Figure 4c. Additionally, an apparent electron loss occurs from these ligand-anchoring Ir sites to the acetylene moieties (>0.14 electrons), while the charge density of neighboring Ir sites remains mostly unchanged (Table S3). Notably, such a trend of electron loss is consistent with their ΔG_{H*} variation. Figure 4d shows the ΔG_{H*} and interfacial charge transfer of the four different Ir anchoring sites in Ir−C≡ that are highlighted in the inset to Figure 4a, where the excellent linear relationship ($R^2 = 0.996$) suggests a strong correlation between the intrinsic HER activity and change in local charge density. One of these ligand-anchoring Ir sites is highlighted in Figure S13 and exhibits an extremely low $|\Delta G_{H*}|$ of only 0.015 eV. Taken together, these results suggest that the ligand-anchoring Ir atoms in Ir−C≡ were most likely responsible for the remarkable HER performance.

To understand the mechanistic origin of the enhanced OER performance, the Gibbs free energy of O* adsorption (ΔG_{O*})

was calculated to examine the interaction between Ir and O species. Interestingly, O* tends to adsorb onto the various Ir slabs in a tridentate mode with one of the Ir sites also bonded to the organic ligand (Figure S14), and the corresponding ΔG_{O*} on the ligand-anchoring Ir atoms shows an apparent difference, as compared to that on the bare Ir(111) slab (Figure S15), −1.457 eV for Ir═N, −1.881 eV for Ir−C≡, −2.058 eV for Ir−S, and −2.300 eV for Ir(111). This implies that the capping ligands effectively stabilize the Ir nanoparticles against oxidation, and the stabilization varies in the order of Ir═N > Ir−C≡ > Ir−S > Ir(111).[27] This is consistent with the metal-to-ligand charge transfer observed in both XPS and DFT measurements (Figure 2).[22] As mentioned earlier, low-valence Ir is preferred for OER.[21,26] Thus, Ir═N and Ir−C≡ are expected to have a better OER performance than Ir−S and Ir/C, in good agreement with results from experimental measurements (Figures 3 and S7).

To gain further mechanistic insights, the reaction barrier of water dissociation, which has been recognized as a critical rate-determining step in OER,[65] was calculated using the nudged elastic band (NEB) method.[66,67] From Figure S16, one can see that the reaction pathway is similar on Ir−C≡, Ir═N, Ir−S, and Ir(111), where water molecules approach the Ir surface and become dissociated into *H and *OH, and the intermediates are adsorbed onto two neighboring Ir atoms in a vertical configuration. The corresponding reaction free energy diagrams of water dissociation are shown in Figure 5,
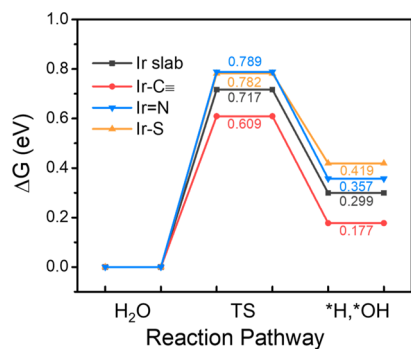

Figure 5. Free energy diagram of water dissociation on Ir(111), Ir−C≡, Ir═N, and Ir−S (Figure S15). TS denotes the transition state. The initial states (H₂O) of all samples are set to zero for comparison of their reaction energy barriers.

where Ir−C≡ can be seen to exhibit an energy barrier of only 0.609 eV, markedly lower than those of Ir═N (0.789 eV), Ir−S (0.782 eV), and Ir(111) slab (0.717 eV). This suggests that Ir−C≡ is the most efficient in water dissociation among the series of samples, in excellent agreement with experimental findings (Figures 3 and S7).

CONCLUSIONS

In summary, when Ir nanoparticles were functionalized with acetylene derivatives, the conjugated metal−ligand interfacial bonding interactions were found to lead to effective charge transfer from the Ir core to the acetylene moieties, which significantly enhanced the HER and OER activity in both acidic and alkaline media because of weakened binding of H and O intermediates, in comparison to leading results of relevant catalysts reported recently in the literature. Of particular note is that the alkaline HER and OER activity was even better than that of commercial Ir/C and Pt/C

benchmarks. Indeed the acetylene-functionalized Ir nanoparticles could be used as effective bifunctional catalysts for full water splitting and significantly outperformed commercial benchmarks. Note that the enhancement was lesser with Ir nanoparticles capped with other ligands such as mercapto and nitrene derivatives because of limited interfacial charge transfer. Consistent results were obtained in DFT calculations. Results from this study highlight the significance of deliberate interfacial engineering in the manipulation of the electronic properties of metal nanoparticles and hence their electro-catalytic activity toward important reactions in electrochemical energy technologies.

EXPERIMENTAL SECTION

Chemicals. Iridium(III) chloride (IrCl₃, 53−56%, Arcos), 1,2-propanediol (>99.5%, Acros), sodium acetate trihydrate (NaOAc·3H₂O, MC&B), EPA (97%, Arcos), EPT (>97%, TCI America), and DBSA (>88%, Aldrich) were used as received. Solvents were purchased from typical commercial sources and used without further purification. Water was purified using a Barnstead Nanopure water system (18.3 MΩ· cm).

Nanoparticle Synthesis. Organically capped iridium nanoparticles were synthesized by adopting a procedure reported previously.[43,44] Briefly, 0.15 mmol IrCl₃ and 86 mg of NaOAc·3H₂O were dissolved in 100 mL of 1,2-propanediol under sonication. After refluxing at 165 °C under vigorous stirring for 2 h, the solution color was found to become dark brown, signifying the formation of Ir nanoparticles. After the solution was cooled down to 60 °C, select organic ligands were added for surface functionalization. Specifically, for EPA and EPT surface functionalization, 4.5 mmol EPA or EPT in 25 mL of toluene was added into the above-mentioned Ir nanoparticle solution under refluxing overnight. The Ir nanoparticles were found to transfer to the toluene phase, which was collected with a separatory funnel and rinsed with methanol five times, affording purified nanoparticles that were denoted as Ir−C≡ and Ir−S for EPA- and EPT-functionalized Ir nanoparticles, respectively.

To prepare nitrene-functionalized Ir (Ir═N) nanoparticles,[48] 0.56 mmol DBSA and 20 mL of *sec*-butylbenzene were added into the Ir nanoparticles solution at 60 °C under magnetic stirring for 1 h. The azide ligands were adsorbed on the nanoparticle surface, resulting in the transfer of the nanoparticles to the *sec*-butylbenzene phase. The *sec*-butylbenzene phase was then collected and refluxed for 24 h at 165 °C, where nitrene radicals were generated by thermolysis of the azide moiety and attached onto the Ir nanoparticle surface, forming Ir═N interfacial bonds. The nanoparticles were then collected and rinsed with acetonitrile five times.

Characterizations. TEM images were acquired with a Philips CM 300 operated at 300 kV. FTIR spectra were collected with a PerkinElmer FTIR spectrometer (Spectrum One), where the samples were prepared by drop casting the nanoparticle solutions in dichloromethane onto a NaCl disk. UV−vis absorption measurements were carried out with a PerkinElmer Lambda 35 UV−vis spectrometer, and photo-luminescence studies were performed with a PTI fluorospec-trometer. XPS measurements were carried out with a Phi X-tool XPS instrument, where the binding energy was calibrated against that of C 1s.

Electrochemistry. The electrocatalytic performance of the organically capped Ir nanoparticles toward HER and OER was examined in a three-electrode system with a CHI 760E electrochemical workstation, where Ag/AgCl (1 M KCl) was used as the reference electrode and a graphite rod was used as the counter electrode. The Ag/AgCl electrode was calibrated against a reversible hydrogen electrode (RHE) and all potentials in the present study were referenced to this RHE. Catalyst inks were prepared by adding 1 mg of the Ir nanoparticles prepared above and 4 mg of carbon black (Vulcan XC-72R) into a mixture of toluene (500 μL), isopropanol (490 μL), and 100% Nafion (10 μL). A total of 10 μL of the catalyst ink was then dropcast onto the surface of a clean glassy carbon electrode (geometric surface area 0.246 cm^2) at a catalyst loading of $\sim$40 μg_{IrNPs} cm^{-2}. Commercial 20% Ir/C was used as the benchmark catalyst and loaded on the glassy carbon electrode in the same fashion at the mass loading of 40 μg_{Ir} cm^{-2}.

Linear sweep voltammograms were collected in both 1 M KOH and 0.5 M H$_2$SO$_4$ at the potential scanning rate of 10 mV s^{-1} and 90% iR compensation. EIS studies were performed within the frequency range of 0.1 Hz to 100 kHz, at the potential of -50 mV for HER and $+1.55$ V for OER in 0.5 M H$_2$SO$_4$ and -100 mV for HER and $+1.55$ V for OER in 1 M KOH.

Full water splitting was performed in a two-electrode system, where the Ir nanoparticles prepared above were used as both the anode and cathode catalysts at the mass loading of $\sim$0.7 mg$_{IrNPs}$ cm^{-2}. As a comparison, commercial Ir/C electrodes at the same mass loading were prepared. The current–voltage curves were collected at the potential scanning rate of 10 mV s^{-1}. Durability tests were carried out by chronoamperometric (CA) measurements for 20 h at the respective E_{10}, where the electrolytes were replaced after 10 h.

Theoretical Study. First-principles computations were performed using Quantum ESPRESSO, an open-source plane-wave code.[68] A 4 × 4 unit cell with 48 atoms was used to build an Ir(111) slab supercell, where periodic image interactions were removed by setting a vacuum of 14 Å. A cutoff of 40 and 240 Ry for kinetics and charge density was chosen with the ultrasoft pseudopotential.[69] The total energy of the Monkhorst–Pack 3 × 3 × 1 K-point grid in the supercell was calculated at the convergence level of 1 meV per atom. The smearing parameter was set at 0.01 Ry in the Marzari–Vanderbilt smearing for all calculations.[70] For geometric relaxation, the convergence was 10^{-8} Ry of the electronic energy and 10^{-4} au for the total force. The dipole correction was added by applying a finite field to the bare ionic potential for all calculations involving ligand modification. Density functional perturbation theory[71] was employed to calculate the phonon frequency as inputs for entropy and zero-point energy. The implicit solvation energy correction was applied with the solvation model CANDLE[72] that has been shown to be suitable for various surfaces, with the open-source code JDFTx.[73,74] The energy barrier calculation was carried out using the NEB method.[66,67]

■ ASSOCIATED CONTENT

ⓢ Supporting Information

The Supporting Information is available free of charge at https://pubs.acs.org/doi/10.1021/acscatal.0c03747.

    Additional experimental and computational data (PDF)

    Production of a large number of bubbles on both the cathode and anode (MP4)

■ AUTHOR INFORMATION

Corresponding Authors

Yuan Ping − *Department of Chemistry and Biochemistry, University of California, Santa Cruz, California 95064, United States;* ⓞ orcid.org/0000-0002-0123-3389; Email: yuanping@ucsc.edu

Shaowei Chen − *Department of Chemistry and Biochemistry, University of California, Santa Cruz, California 95064, United States;* ⓞ orcid.org/0000-0002-3668-8551; Email: shaowei@ucsc.edu

Authors

Yi Peng − *Department of Chemistry and Biochemistry, University of California, Santa Cruz, California 95064, United States;* ⓞ orcid.org/0000-0002-5319-1336

Qiming Liu − *Department of Chemistry and Biochemistry, University of California, Santa Cruz, California 95064, United States;* ⓞ orcid.org/0000-0001-5839-5453

Bingzhang Lu − *Department of Chemistry and Biochemistry, University of California, Santa Cruz, California 95064, United States*

Ting He − *Department of Chemistry and Biochemistry, University of California, Santa Cruz, California 95064, United States; College of Chemistry and Chemical Engineering, Central South University, Changsha, Hunan 410083, China*

Forrest Nichols − *Department of Chemistry and Biochemistry, University of California, Santa Cruz, California 95064, United States*

Xiao Hu − *School of Environment and Energy, South China University of Technology, Guangzhou, Guangdong 510006, China*

Tiffanie Huang − *Department of Chemistry and Biochemistry, University of California, Santa Cruz, California 95064, United States*

Grace Huang − *Department of Chemistry and Biochemistry, University of California, Santa Cruz, California 95064, United States*

Lizette Guzman − *Department of Chemistry and Biochemistry, University of California, Santa Cruz, California 95064, United States*

Complete contact information is available at:
https://pubs.acs.org/10.1021/acscatal.0c03747

Author Contributions

Y. Peng, Q.L., and B.L. contributed equally. The manuscript was written through contributions of all authors. All authors have given approval to the final version of the manuscript.

Notes

The authors declare no competing financial interest.

■ REFERENCES

(1) Chen, S.; Qiao, S.-Z. Hierarchically Porous Nitrogen-Doped Graphene-NiCo2O4 Hybrid Paper as an Advanced Electrocatalytic Water-Splitting Material. *ACS Nano* **2013**, *7*, 10190−10196.

(2) Wu, Z.; Wang, Z.; Geng, F. Radially Aligned Hierarchical Nickel/Nickel-Iron (Oxy)hydroxide Nanotubes for Efficient Electrocatalytic Water Splitting. *ACS Appl. Mater. Interfaces* **2018**, *10*, 8585−8593.

(3) Pi, Y.; Shao, Q.; Wang, P.; Guo, J.; Huang, X. General Formation of Monodisperse IrM (M = Ni, Co, Fe) Bimetallic Nanoclusters as Bifunctional Electrocatalysts for Acidic Overall Water Splitting. *Adv. Funct. Mater.* **2017**, *27*, 1700886.

(4) Zhong, H.-X.; Wang, J.; Zhang, Q.; Meng, F.; Bao, D.; Liu, T.; Yang, X.-Y.; Chang, Z.-W.; Yan, J.-M.; Zhang, X.-B. In Situ Coupling FeM (M = Ni, Co) with Nitrogen-Doped Porous Carbon toward Highly Efficient Trifunctional Electrocatalyst for Overall Water Splitting and Rechargeable Zn-Air Battery. *Adv. Sustain. Syst.* **2017**, *1*, 1700020.

(5) Peng, Y.; Hirata, E. Y.; Pan, W.; Chen, L.; Lu, J. E.; Chen, S. Intraparticle Charge Delocalization through Conjugated Metal-Ligand Interfacial Bonds: Effects of Metal d Electrons. *Chin. J. Chem. Phys.* **2018**, *31*, 433−438.

(6) You, B.; Sun, Y. Innovative Strategies for Electrocatalytic Water Splitting. *Acc. Chem. Res.* **2018**, *51*, 1571−1580.

(7) Chen, P.; Tong, Y.; Wu, C.; Xie, Y. Surface/Interfacial Engineering of Inorganic Low-Dimensional Electrode Materials for Electrocatalysis. *Acc. Chem. Res.* **2018**, *51*, 2857−2866.

(8) Zhang, J.; Zhang, Q.; Feng, X. Support and Interface Effects in Water-Splitting Electrocatalysts. *Adv. Mater.* **2019**, *31*, 1808167.

(9) Li, Z.; Niu, W.; Yang, Z.; Kara, A.; Wang, Q.; Wang, M.; Gu, M.; Feng, Z.; Du, Y.; Yang, Y. Boosting alkaline hydrogen evolution: the dominating role of interior modification in surface electrocatalysis. *Energy Environ. Sci.* **2020**, *13*, 3110−3118.

(10) Yao, Q.; Huang, B.; Zhang, N.; Sun, M.; Shao, Q.; Huang, X. Channel-Rich RuCu Nanosheets for pH-Universal Overall Water Splitting Electrocatalysis. *Angew. Chem., Int. Ed.* **2019**, *58*, 13983−13988.

(11) Mamaca, N.; Mayousse, E.; Arrii-Clacens, S.; Napporn, T. W.; Servat, K.; Guillet, N.; Kokoh, K. B. Electrochemical activity of ruthenium and iridium based catalysts for oxygen evolution reaction. *Appl. Catal., B* **2012**, *111−112*, 376−380.

(12) AlYami, N. M.; LaGrow, A. P.; Joya, K. S.; Hwang, J.; Katsiev, K.; Anjum, D. H.; Losovyj, Y.; Sinatra, L.; Kim, J. Y.; Bakr, O. M. Tailoring ruthenium exposure to enhance the performance of fcc platinum@ruthenium core-shell electrocatalysts in the oxygen evolution reaction. *Phys. Chem. Chem. Phys.* **2016**, *18*, 16169−16178.

(13) Cheng, N.; Stambula, S.; Wang, D.; Banis, M.; Liu, J.; Riese, A.; Xiao, B.; Li, R.; Sham, T.; Liu, L.; Botton, G.; Sun, X. Platinum single-atom and cluster catalysis of the hydrogen evolution reaction. *Nat. Commun.* **2016**, *7*, 13638.

(14) Zheng, Y.; Jiao, Y.; Zhu, Y.; Li, L. H.; Han, Y.; Chen, Y.; Jaroniec, M.; Qiao, S.-Z. High Electrocatalytic Hydrogen Evolution

(15) Mahmood, J.; Li, F.; Jung, S.-M.; Okyay, M. S.; Ahmad, I.; Kim, S.-J.; Park, N.; Jeong, H. Y.; Baek, J.-B. An efficient and pH-universal ruthenium-based catalyst for the hydrogen evolution reaction. *Nat. Nanotechnol.* **2017**, *12*, 441−446.

(16) Zheng, J. Binary platinum alloy electrodes for hydrogen and oxygen evolutions by seawater splitting. *Appl. Surf. Sci.* **2017**, *413*, 72−82.

(17) Qiu, T.; Liang, Z.; Guo, W.; Gao, S.; Qu, C.; Tabassum, H.; Zhang, H.; Zhu, B.; Zou, R.; Shao-Horn, Y. Highly exposed ruthenium-based electrocatalysts from bimetallic metal-organic frameworks for overall water splitting. *Nano Energy* **2019**, *58*, 1−10.

(18) Park, J.; Sa, Y. J.; Baik, H.; Kwon, T.; Joo, S. H.; Lee, K. Iridium-Based Multimetallic Nanoframe@Nanoframe Structure: An Efficient and Robust Electrocatalyst toward Oxygen Evolution Reaction. *ACS Nano* **2017**, *11*, 5500−5509.

(19) Zhang, J.; Wang, G.; Liao, Z.; Zhang, P.; Wang, F.; Zhuang, X.; Zschech, E.; Feng, X. Iridium nanoparticles anchored on 3D graphite foam as a bifunctional electrocatalyst for excellent overall water splitting in acidic solution. *Nano Energy* **2017**, *40*, 27−33.

(20) Xue, Q.; Gao, W.; Zhu, J.; Peng, R.; Xu, Q.; Chen, P.; Chen, Y. Carbon nanobowls supported ultrafine iridium nanocrystals: An active and stable electrocatalyst for the oxygen evolution reaction in acidic media. *J. Colloid Interface Sci.* **2018**, *529*, 325−331.

(21) Wu, X.; Feng, B.; Li, W.; Niu, Y.; Yu, Y.; Lu, S.; Zhong, C.; Liu, P.; Tian, Z.; Chen, L.; Hu, W.; Li, C. M. Metal-support interaction boosted electrocatalysis of ultrasmall iridium nanoparticles supported on nitrogen doped graphene for highly efficient water electrolysis in acidic and alkaline media. *Nano Energy* **2019**, *62*, 117−126.

(22) You, H.; Wu, D.; Chen, Z.-n.; Sun, F.; Zhang, H.; Chen, Z.; Cao, M.; Zhuang, W.; Cao, R. Highly Active and Stable Water Splitting in Acidic Media Using a Bifunctional Iridium/Cucurbit[6]-uril Catalyst. *ACS Energy Lett.* **2019**, *4*, 1301−1307.

(23) Zhao, Y.; Luo, M.; Chu, S.; Peng, M.; Liu, B.; Wu, Q.; Liu, P.; de Groot, F. M. F.; Tan, Y. 3D nanoporous iridium-based alloy microwires for efficient oxygen evolution in acidic media. *Nano Energy* **2019**, *59*, 146−153.

(24) Norskov, J. K.; Bligaard, T.; Logadottir, A.; Kitchin, J. R.; Chen, J. G.; Pandelov, S.; Norskov, J. K. Trends in the exchange current for hydrogen evolution. *J. Electrochem. Soc.* **2005**, *152*, J23−J26.

(25) Jiao, Y.; Zheng, Y.; Jaroniec, M.; Qiao, S. Z. Design of electrocatalysts for oxygen- and hydrogen-involving energy conversion reactions. *Chem. Soc. Rev.* **2015**, *44*, 2060−2086.

(26) Li, T.; Kasian, O.; Cherevko, S.; Zhang, S.; Geiger, S.; Scheu, C.; Felfer, P.; Raabe, D.; Gault, B.; Mayrhofer, K. J. J. Atomic-scale insights into surface species of electrocatalysts in three dimensions. *Nat. Catal.* **2018**, *1*, 300−305.

(27) Montemore, M. M.; van Spronsen, M. A.; Madix, R. J.; Friend, C. M. O2 Activation by Metal Surfaces: Implications for Bonding and Reactivity on Heterogeneous Catalysts. *Chem. Rev.* **2018**, *118*, 2816−2862.

(28) Kwon, T.; Hwang, H.; Sa, Y. J.; Park, J.; Baik, H.; Joo, S. H.; Lee, K. Cobalt Assisted Synthesis of IrCu Hollow Octahedral Nanocages as Highly Active Electrocatalysts toward Oxygen Evolution Reaction. *Adv. Funct. Mater.* **2017**, *27*, 1604688.

(29) Ahn, S. H.; Tan, H.; Haensch, M.; Liu, Y.; Bendersky, L. A.; Moffat, T. P. Self-terminated electrodeposition of iridium electrocatalysts. *Energy Environ. Sci.* **2015**, *8*, 3557−3562.

(30) Jiang, B.; Guo, Y.; Kim, J.; Whitten, A. E.; Wood, K.; Kani, K.; Rowan, A. E.; Henzie, J.; Yamauchi, Y. Mesoporous Metallic Iridium Nanosheets. *J. Am. Chem. Soc.* **2018**, *140*, 12434−12441.

(31) Pi, Y.; Zhang, N.; Guo, S.; Guo, J.; Huang, X. Ultrathin Laminar Ir Superstructure as Highly Efficient Oxygen Evolution Electrocatalyst in Broad pH Range. *Nano Lett.* **2016**, *16*, 4424−4430.

(32) Yin, L.; Yang, T.; Ding, X.; He, M.; Wei, W.; Yu, T.; Zhao, H. Synthesis of phosphorus-iridium nanocrystals and their superior electrocatalytic activity for oxygen evolution reaction. *Electrochem. Commun.* **2018**, *94*, 59−63.

(33) Sun, X.; Liu, F.; Chen, X.; Li, C.; Yu, J.; Pan, M. Iridium-doped ZIFs-derived porous carbon-coated IrCo alloy as competent bifunctional catalyst for overall water splitting in acid medium. *Electrochim. Acta* **2019**, *307*, 206−213.

(34) Wang, C.; Sui, Y.; Xiao, G.; Yang, X.; Wei, Y.; Zou, G.; Zou, B. Synthesis of Cu-Ir nanocages with enhanced electrocatalytic activity for the oxygen evolution reaction. *J. Mater. Chem. A* **2015**, *3*, 19669−19673.

(35) Zhu, J.; Lyu, Z.; Chen, Z.; Xie, M.; Chi, M.; Jin, W.; Xia, Y. Facile Synthesis and Characterization of Pd@Ir-nL (n=1-4) Core-Shell Nanocubes for Highly Efficient Oxygen Evolution in Acidic Media. *Chem. Mater.* **2019**, *31*, 5867−5875.

(36) Fu, L.; Hu, X.; Li, Y.; Cheng, G.; Luo, W. IrW nanobranches as an advanced electrocatalyst for pH-universal overall water splitting. *Nanoscale* **2019**, *11*, 8898−8905.

(37) Li, D.; Zong, Z.; Tang, Z.; Liu, Z.; Chen, S.; Tian, Y.; Wang, X. Total Water Splitting Catalyzed by Co@Ir Core-Shell Nanoparticles Encapsulated in Nitrogen-Doped Porous Carbon Derived from Metal Organic Frameworks. *ACS Sustain. Chem. Eng.* **2018**, *6*, 5105−5114.

(38) Pu, Z.; Zhao, J.; Amiinu, I. S.; Li, W.; Wang, M.; He, D.; Mu, S. A universal synthesis strategy for P-rich noble metal diphosphide-based electrocatalysts for the hydrogen evolution reaction. *Energy Environ. Sci.* **2019**, *12*, 952−957.

(39) Hu, P.; Chen, L.; Kang, X.; Chen, S. Surface Functionalization of Metal Nanoparticles by Conjugated Metal-Ligand Interfacial Bonds: Impacts on Intraparticle Charge Transfer. *Acc. Chem. Res.* **2016**, *49*, 2251−2260.

(40) Tang, Q.; Jiang, D.-e. Comprehensive View of the Ligand Gold Interface from First Principles. *Chem. Mater.* **2017**, *29*, 6908−6915.

(41) Zhou, Z.-Y.; Kang, X.; Song, Y.; Chen, S. Ligand-Mediated Electrocatalytic Activity of Pt Nanoparticles for Oxygen Reduction Reactions. *J. Phys. Chem. C* **2012**, *116*, 10592−10598.

(42) Hu, P.; Chen, L.; Deming, C. P.; Lu, J.-E.; Bonny, L. W.; Chen, S. Effects of para-substituents of styrene derivatives on their chemical reactivity on platinum nanoparticle surfaces. *Nanoscale* **2016**, *8*, 12013−12021.

(43) Hu, P.; Chen, L.; Deming, C. P.; Kang, X.; Chen, S. Nanoparticle-Mediated Intervalence Charge Transfer: Core-Size Effects. *Angew. Chem., Int. Ed.* **2016**, *55*, 1455−1459.

(44) Kang, X.; Zuckerman, N. B.; Konopelski, J. P.; Chen, S. Alkyne-Functionalized Ruthenium Nanoparticles: Ruthenium-Vinylidene Bonds at the Metal-Ligand Interface. *J. Am. Chem. Soc.* **2012**, *134*, 1412−1415.

(45) Wang, X.; Zhuang, J.; Peng, Q.; Li, Y. A general strategy for nanocrystal synthesis. *Nature* **2005**, *437*, 121−124.

(46) Creighton, J. A.; Eadon, D. G. Ultraviolet−visible absorption spectra of the colloidal metallic elements. *J. Chem. Soc., Faraday Trans.* **1991**, *87*, 3881−3891.

(47) Hu, P.; Chen, L.; Deming, C. P.; Bonny, L. W.; Lee, H.-W.; Chen, S. Identification of the formation of metal-vinylidene interfacial bonds of alkyne-capped platinum nanoparticles by isotopic labeling. *Chem. Commun.* **2016**, *52*, 11631−11633.

(48) Kang, X.; Song, Y.; Chen, S. Nitrene-functionalized ruthenium nanoparticles. *J. Mater. Chem.* **2012**, *22*, 19250−19257.

(49) Deming, C. P.; Kang, X.; Liu, K.; Chen, S. Nitrene-functionalized ruthenium nanoparticles: Selective manipulation of nanoparticle electronic conductivity by vinyl derivatives. *Sens. Actuators, B* **2014**, *194*, 319−324.

(50) Marinova, T. S.; Kostov, K. L. Adsorption of acetylene and ethylene on a clean Ir (111) surface. *Surf. Sci.* **1987**, *181*, 573−585.

(51) Lima, F. H. B.; Zhang, J.; Shao, M. H.; Sasaki, K.; Vukmirovic, M. B.; Ticianelli, E. A.; Adzic, R. R. Catalytic activity-d-band center correlation for the O-2 reduction reaction on platinum in alkaline solutions. *J. Phys. Chem. C* **2007**, *111*, 404−410.

(52) Stamenkovic, V. R.; Fowler, B.; Mun, B. S.; Wang, G.; Ross, P. N.; Lucas, C. A.; Markovic, N. M. Improved oxygen reduction activity on Pt3Ni(111) via increased surface site availability. *Science* **2007**, *315*, 493−497.

(53) Toyoda, E.; Jinnouchi, R.; Hatanaka, T.; Morimoto, Y.; Mitsuhara, K.; Visikovskiy, A.; Kido, Y. The d-Band Structure of Pt Nanoclusters Correlated with the Catalytic Activity for an Oxygen Reduction Reaction. *J. Phys. Chem. C* **2011**, *115*, 21236−21240.

(54) Lu, B.; Guo, L.; Wu, F.; Peng, Y.; Lu, J.; Smart, T. J.; Wang, N.; Finfrock, Y.; Morris, D.; Zhang, P.; Li, N.; Gao, P.; Ping, Y.; Chen, S. Ruthenium atomically dispersed in carbon outperforms platinum toward hydrogen evolution in alkaline media. *Nat. Commun.* **2019**, *10*, 631.

(55) Bhardwaj, M.; Balasubramaniam, R. Uncoupled non-linear equations method for determining kinetic parameters in case of hydrogen evolution reaction following Volmer−Heyrovsky−Tafel mechanism and Volmer−Heyrovsky mechanism. *Int. J. Hydrogen Energy* **2008**, *33*, 2178−2188.

(56) de Chialvo, M. R. G.; Chialvo, A. C. Hydrogen evolution reaction: analysis of the Volmer-Heyrovsky-Tafel mechanism with a generalized adsorption model. *J. Electroanal. Chem.* **1994**, *372*, 209−223.

(57) Suntivich, J.; May, K. J.; Gasteiger, H. A.; Goodenough, J. B.; Shao-Horn, Y. A Perovskite Oxide Optimized for Oxygen Evolution Catalysis from Molecular Orbital Principles. *Science* **2011**, *334*, 1383−1385.

(58) McCrory, C. C. L.; Jung, S.; Peters, J. C.; Jaramillo, T. F. Benchmarking Heterogeneous Electrocatalysts for the Oxygen Evolution Reaction. *J. Am. Chem. Soc.* **2013**, *135*, 16977−16987.

(59) Nakagawa, T.; Beasley, C. A.; Murray, R. W. Efficient Electro-Oxidation of Water near Its Reversible Potential by a Mesoporous IrOx Nanoparticle Film. *J. Phys. Chem. C* **2009**, *113*, 12958−12961.

(60) Wang, J.; Cui, W.; Liu, Q.; Xing, Z.; Asiri, A. M.; Sun, X. Recent Progress in Cobalt-Based Heterogeneous Catalysts for Electrochemical Water Splitting. *Adv. Mater.* **2016**, *28*, 215−230.

(61) Anantharaj, S.; Ede, S. R.; Sakthikumar, K.; Karthick, K.; Mishra, S.; Kundu, S. Recent Trends and Perspectives in Electrochemical Water Splitting with an Emphasis on Sulfide, Selenide, and Phosphide Catalysts of Fe, Co, and Ni: A Review. *ACS Catal.* **2016**, *6*, 8069−8097.

(62) Hagedorn, C. J.; Weiss, M. J.; Weinberg, W. H. Dissociative chemisorption of hydrogen on Ir(111): Evidence for terminal site adsorption. *Phys. Rev. B: Condens. Matter Mater. Phys.* **1999**, *60*, 14016−14018.

(63) Zhang, F.; Fang, J.; Huang, L.; Sun, W.; Lin, Z.; Shi, Z.; Kang, X.; Chen, S. Alkyne-Functionalized Ruthenium Nanoparticles: Impact of Metal-Ligand Interfacial Bonding Interactions on the Selective Hydrogenation of Styrene. *ACS Catal.* **2019**, *9*, 98−104.

(64) Gao, J.; Ma, H.; Lv, X.; Yan, T.; Li, N.; Cao, W.; Wei, Q. A novel electrochemical immunosensor using β-cyclodextrins functionalized silver supported adamantine-modified glucose oxidase as labels for ultrasensitive detection of alpha-fetoprotein. *Anal. Chim. Acta* **2015**, *893*, 49−56.

(65) Ping, Y.; Nielsen, R. J.; Goddard, W. A., III The reaction mechanism with free energy barriers at constant potentials for the oxygen evolution reaction at the IrO2 (110) surface. *J. Am. Chem. Soc.* **2017**, *139*, 149−155.

(66) Giannozzi, P.; Andreussi, O.; Brumme, T.; Bunau, O.; Buongiorno Nardelli, M.; Calandra, M.; Car, R.; Cavazzoni, C.; Ceresoli, D.; Cococcioni, M.; Colonna, N.; Carnimeo, I.; Dal Corso, A.; de Gironcoli, S.; Delugas, P.; DiStasio, R. A.; Ferretti, A.; Floris, A.; Fratesi, G.; Fugallo, G.; Gebauer, R.; Gerstmann, U.; Giustino, F.; Gorni, T.; Jia, J.; Kawamura, M.; Ko, H.-Y.; Kokalj, A.; Küçükbenli, E.; Lazzeri, M.; Marsili, M.; Marzari, N.; Mauri, F.; Nguyen, N. L.; Nguyen, H.-V.; Otero-de-la-Roza, A.; Paulatto, L.; Poncé, S.; Rocca, D.; Sabatini, R.; Santra, B.; Schlipf, M.; Seitsonen, A. P.; Smogunov, A.; Timrov, I.; Thonhauser, T.; Umari, P.; Vast, N.; Wu, X.; Baroni, S. Advanced capabilities for materials modelling with Quantum ESPRESSO. *J. Phys.: Condens. Matter* **2017**, *29*, 465901.

(67) Henkelman, G.; Jónsson, H. A dimer method for finding saddle points on high dimensional potential surfaces using only first derivatives. *J. Chem. Phys.* **1999**, *111*, 7010−7022.

(68) Giannozzi, P.; Baroni, S.; Bonini, N.; Calandra, M.; Car, R.; Cavazzoni, C.; Ceresoli, D.; Chiarotti, G. L.; Cococcioni, M.; Dabo, I.; Dal Corso, A.; de Gironcoli, S.; Fabris, S.; Fratesi, G.; Gebauer, R.; Gerstmann, U.; Gougoussis, C.; Kokalj, A.; Lazzeri, M.; Martin-Samos, L.; Marzari, N.; Mauri, F.; Mazzarello, R.; Paolini, S.; Pasquarello, A.; Paulatto, L.; Sbraccia, C.; Scandolo, S.; Sclauzero, G.; Seitsonen, A. P.; Smogunov, A.; Umari, P.; Wentzcovitch, R. M. QUANTUM ESPRESSO: a modular and open-source software project for quantum simulations of materials. *J. Phys.: Condens. Matter* **2009**, *21*, 395502.

(69) Garrity, K. F.; Bennett, J. W.; Rabe, K. M.; Vanderbilt, D. Pseudopotentials for high-throughput DFT calculations. *Comput. Mater. Sci.* **2014**, *81*, 446−452.

(70) Marzari, N.; Vanderbilt, D.; De Vita, A.; Payne, M. C. Thermal Contraction and Disordering of the Al(110) Surface. *Phys. Rev. Lett.* **1999**, *82*, 3296−3299.

(71) Baroni, S.; De Gironcoli, S.; Dal Corso, A.; Giannozzi, P. Phonons and related crystal properties from density-functional perturbation theory. *Rev. Mod. Phys.* **2001**, *73*, 515.

(72) Sundararaman, R.; Goddard, W. A., III The charge-asymmetric nonlocally determined local-electric (CANDLE) solvation model. *J. Chem. Phys.* **2015**, *142*, 064107.

(73) Petrosyan, S.; Briere, J.-F.; Roundy, D.; Arias, T. A. Joint density-functional theory for electronic structure of solvated systems. *Phys. Rev. B: Condens. Matter Mater. Phys.* **2006**, *75*, 205105.

(74) Ping, Y.; Sundararaman, R.; Goddard, W. A., III Solvation effects on the band edge positions of photocatalysts from first principles. *Phys. Chem. Chem. Phys.* **2015**, *17*, 30499−30509.